Erschienen in: Advanced Materials ; 24 (2012), 10. - S. 1309-1315
https://dx.doi.org/10.1002/adma.201104605

Synthesis and Optical Properties of Mesoporous β-$Co(OH)_2$/Brilliant Blue G (G250) Hybrid Hierarchical Structures

*Huai-Ping Cong, Xiao-Chen Ren, Hong-Bin Yao, Ping Wang, Helmut Cölfen, and Shu-Hong Yu**

Cobalt hydroxide is a well-known lamellar crystalline compound, which has attracted much interest and is used in a variety of applications such as catalysis,[1] electrochemical[2] and magnetic recording materials.[3] Cobalt hydroxide can be crystallized into two polymorphic forms, α- and β-$Co(OH)_2$ with hexagonal layered structures.[4] The pink β-phase assembly shows a brucite-like structure with cobalt ions occupying the alternate rows of octahedral sites, while the hydrotalcite-like metastable α-$Co(OH)_2$ consists of positively charged $Co(OH)_{2-x}$ layers intercalated with various charge balancing anions (e.g. chloride, nitrate, carbonate, etc.), exhibiting a characteristic green/blue color.

The promising properties of the hydroxides are closely associated with their shape and microstructure, such as the surface area and morphology dependent electrochemical capacitance.[5] Therefore, great attention has been paid on the fabrication of large quantities of $Co(OH)_2$ architectures with different morphologies by solution-phase chemical and electrochemical deposition methods. Cobalt hydroxide nanobelts with tunable shapes and sizes were fabricated by a facile hydrothermal route.[6] Hosono et al. achieved the control of the films of brucite-$Co(OH)_2$ nanorods and hydrotalcite-$Co(OH)_2$ nanosheets in different solvents.[7] Lou and co-workers reported the unique needlelike cobalt hydroxides and their transformation to cobalt oxide nanotubes with ultrahigh electrochemical capacity as lithium-ion battery electrodes.[8] Various forms of butterfly-like β-$Co(OH)_2$ composed of nanoplates or nanorods can be constructed via ethylenediamine-mediated synthesis.[9] Recently, another triangle tape-like cobalt hydroxide has been synthesized by a solid-state crystal reconstruction approach.[10] Furthermore, 3D hierarchical structures were also reported, including microspheres, coral-, and flower-like nanostructures.[11]

Mesocrystal, a short term for mesoscopically structured crystal, has been an exciting example of nonclassical crystallization in the past years, not through the ion-ion attachment, but by a modular nanoparticle building-block route.[12] Mesocrystals are composed of non-spherical nanoparticles arranged in a common crystallographic fashion, whose scattering behavior in X-ray and electron diffraction can not be distinguished from a single crystal. In a crystallization reaction, they often serve as intermediates to form the single crystals with typical defects and inclusions. The mesocrystal concept is favorable for a better understanding of biomineralization processes, for example, the assembly of sea urchin spikes and aragonite tablets in nacre in nature.[12c,13] Meanwhile, large quantities of organics and synthetic polyelectrolytes have been applied to control the size and shape of inorganic crystals and induce the formation of mesocrystals with high inner surface area.[14] In such process, it is quite important to stabilize nanoparticle-intermediates by de-emulsification, charge stabilization and magnetism etc,[15] allowing assembly of the intermediates in a non-random pathway.

Meanwhile, mesoporous transition-metal materials have also aroused increasing attention in electrochemical fields due to the high BET surface areas, large pore volumes and channels for ion, atom, and molecule diffusion, not only at the surfaces, but also throughout the bulk.[16] Mesoporous cobalt oxide nanowire arrays were directly grown on various substrates by a mild solution-based template-free method, showing high capacities as the anode for lithium ion batteries.[17] Wang and co-workers fabricated Co_3O_4 electrode materials with an ultrahigh capacitance by a hard template technique.[18] However, there are only very few reports on the direct synthesis of mesoporous cobalt hydroxides.[10,19] A majority of cobalt hydroxides served as the precursors for the further thermal conversion to porous cobalt oxide materials.[7,11c,20]

Nowadays, integrating functional inorganic and organic components into one system is a hot topic due to the desire to explore novel materials with new functionalities in academia and innovative industrial applications.[21] Previously, we demonstrated that complex dye-based hybrid materials with hierarchical structures and new optical functionalities can be fabricated by combining zinc compounds with various dyes.[22]

In this Communication, we first achieved the incorporation of brilliant blue G (G250), an important dye for protein detection and electrophoresis, into brucite-like β-$Co(OH)_2$ to

Dr. H.-P. Cong, X.-C. Ren, H.-B. Yao, P. Wang, Prof. Dr. S. H. Yu
Division of Nanomaterials & Chemistry
Hefei National Laboratory for Physical Sciences at Microscale
Department of Chemistry
The National Synchrotron Radiation Laboratory
University of Science and Technology of China
Hefei 230026, P. R. China
Fax: 0086 551 3603040
E-mail: shyu@ustc.edu.cn
Prof. Dr. H. Cölfen
University of Konstanz
Physical Chemistry
Universitätsstraße 10, Box 714, D-78457 Konstanz, Germany

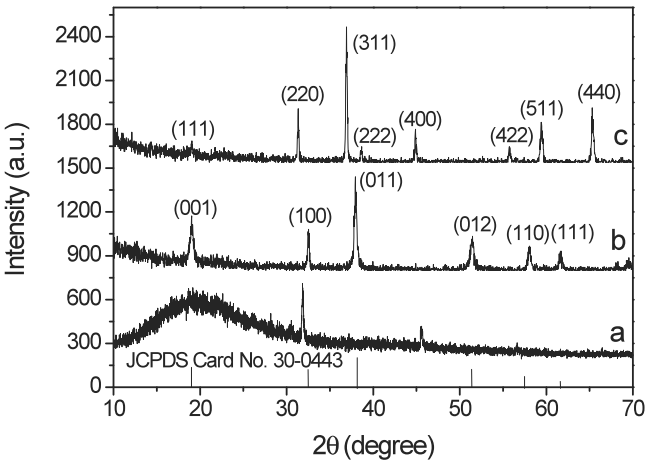

Figure 1. XRD patterns of (a) dye G250; (b) β-$Co(OH)_2$/dye hybrid flowers; (c) the product prepared by heat treatment of β-$Co(OH)_2$/dye hybrid flowers at 800 °C.

construct hierarchical hybrid microstructures with flower shape composed of mesocrystal nanosheets with new optical property via a one-step refluxing approach. The dye G250 induced the formation of cobalt hydroxide mesocrystal sheets and was included in the final hybrid products. The Ostwald ripening formation mechanism of such unique flowerlike β-$Co(OH)_2$ hybrids was clearly revealed and detailed by time-dependent experiments. To the best of our knowledge, it is also a first report on mesoporous β-$Co(OH)_2$/dye composites with quite high surface area through a straightforward synthesis method, which may find application in oxygen reduction reactions and the field of pigments.

The cobalt hydroxide composite with blue color was prepared by refluxing cobalt acetate precursors in ammonia ethanol/water solution in the presence of CTAB and G250 at 140 °C. The powder XRD pattern of the badly-crystallized G250 presents a broad and two other weak peaks in **Figure 1**a, the positions of which are at 19.4°, 31.8°, and 45.6°, respectively. All the diffraction peaks of the hybrid sample as revealed in Figure 1b are well indexed as the brucite-like β-$Co(OH)_2$ according to JCPDS Card No. 30-0443. Here, it is observed that the intrinsic broad peak position of G250 at 19.4° overlapped with that of (001) of β-$Co(OH)_2$. Thus, more characterization is needed to reveal the structure and composition information of the sample.

The morphology and microstructure of the blue-colored β-$Co(OH)_2$ product is shown in SEM and TEM images **Figure 2**a-d. Large quantities of the typical flower-like particles with a size of 8–10 μm were clearly revealed by low-magnified SEM images. A closer observation in Figure 2c displayed that each flower was of hierarchical structure and composed of very thin nanosheets constructed by nanoplates. The microsized mesoporous structure of the β-$Co(OH)_2$ nanosheets was found to be porous and have uniform pores with a size of about 10 nm (Figure 2e). Interestingly, a large porous network structure of nanoparticles was clearly shown on the nanosheet by HRTEM image (Figure 2g), from which the typical (100) crystal plane of β-$Co(OH)_2$ was observed. The corresponding electron diffraction

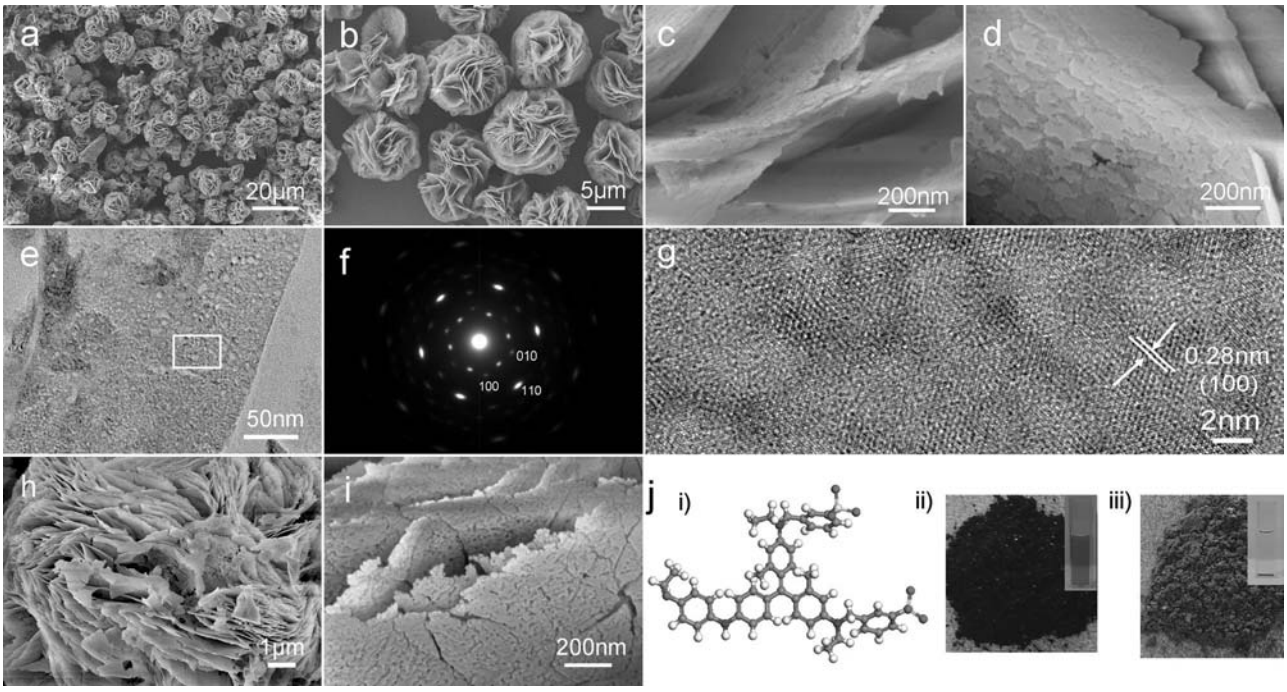

Figure 2. (a-d) SEM images of β-$Co(OH)_2$/dye hybrid flowers with different magnifications. TEM image inserted in (d) showing the mesoporous structure of the sheets; (e) TEM image of the nanosheet in the β-$Co(OH)_2$/dye flower; (f,g) HRTEM image of the white-marked area and corresponding selected area electron diffraction (SAED) pattern; (h,i) Low and high magnified SEM image of the products by the heat treatment of β-$Co(OH)_2$/dye hybrid flowers at 800°C; (j) Geometric structure of G250 molecule, subpanel i); photograph of solid G250 (ii) and solid β-$Co(OH)_2$/G250 composite (iii); the inset shows the ethanol solution of the solid G250 and β-$Co(OH)_2$/G250 composite, respectively.

presented a single-crystal-like alignment of nanoparticles with a spot pattern characteristic (Figure 2f), revealing the formation of mesocrystal.[12a] Based on the previous detailed studies on the mineralization with copolymers and small molecules,[14c,15b,23] β-$Co(OH)_2$ nanoparticles were presumably stabilized by the dye G250 used in this work containing the negative-charged sulfonate groups, which randomly distributed the surrounding of nanoparticle-intermediates through charge interactions and induced the formation of the mesocrystal nanosheets and sustained the porous network.

The N_2 adsorption/desorption isotherm curve and the corresponding pore size distribution plot demonstrate the porous nature of the β-$Co(OH)_2$ flowers (Supporting Information, Figure S1). The Brunauer–Emmett–Teller (BET) surface area was 95.21 m^2/g with an average pore size of 12.9 nm and the Barrett–Joyner–Halenda (BJH) adsorption cumulative pore volume was 0.376 cm^3/g, which coincide well with the results from highly-magnified SEM and TEM observations. Such mesoporous β-$Co(OH)_2$ microstructures are useful for the transportation of ions, atoms and molecules not only at the surfaces, but also through the whole bulk, and the full contact of electrolytes. Thus, it may open up the potential applications in electrochemical catalysis and lithium-ion batteries, etc.

Fourier transform infrared (FTIR) analysis is an important and strong proof to illustrate the composition of the as-prepared β-$Co(OH)_2$ (Supporting Information, Figure S2). The characteristic vibration bands, –C=C, –C–N, $-SO_3$, $-CH_3$, $-CH_2$ and –Ar–H, of the dye G250 were observed in the FTIR spectrum of the flower-like products. The narrow bands at 3632 and 499 cm^{-1} correspond to the υ-OH stretching of the OH groups and Co-OH bending vibration in the brucite-like structure, respectively.[19,24] The wide band centered at 3433 cm^{-1} is attributed to the vibration of hydroxyl groups of water.[25] These results are in a good agreement with the phase analysis of β-$Co(OH)_2$ by XRD pattern and well confirmed the effective incorporation of the dye into the inorganic solid by the present simple one-step refluxing process.

Thermogravimetric (TG) and differential scanning calorimetric (DSC) analysis were carried out in air to reveal the possible effect on the thermal behavior caused by the incorporation of dye with β-$Co(OH)_2$ and the content information of the dye (Supporting Information, Figure S3). Firstly, the measurements were performed in order to show the nature thermal behavior of the pure dye G250. Two dominant weight losses of 77.5 wt% in total due to the thermal decomposition of the dye G250 are observed in the range of 200–700 °C. The corresponding DSC curve shows an exothermal peak centered at 535 and 570 °C. The water-induced weight loss is centralized below 200 °C. Due to the presence of sodium ions in the dye G250, the weight loss is not 100 percent.

A total weight loss of 20 wt% was shown in the TGA-DSC curve of β-$Co(OH)_2$/G250 hybrid flowers (Supporting Information, Figure S3b). The first slight weight loss of about 2.8 wt% below 150 °C was assigned to the elimination of water in the material. As the temperature increased, the distinct mass loss profile exhibits a well-defined decrease at 150–500 °C, due to the thermal decomposition of the sample. After this, no obvious mass loss is observed in the TGA curve anymore. Theoretically, the DSC curve should exhibit an endothermic peak towards the decomposition of cobalt hydroxide to cobalt oxide.[26] However, in our experiment, the typical exothermic peak is observed when the endothermic behavior of the $Co(OH)_2$ decomposition and the exothermic dye decomposition occur simultaneously.[24] Furthermore, compared with the pure G250 and the G250 hybrids, the temperature of the exothermic peak of dye decreased distinctly from 500–700 °C to 150–350 °C, due to the better contact surfaces of the dye well-dispersed on the $Co(OH)_2$ sheets, which favors the effective decomposition in air. The position and type of the thermal peak in the DSC plot of β-$Co(OH)_2$/G250 fully testifies the available inclusion of G250 into β-$Co(OH)_2$. According to the 80 wt% of the residual product and the theoretical value (13.6 wt%) from the decomposition of $Co(OH)_2$ to Co_3O_4, it was calculated that 4.6 wt% of G250 was included in the β-$Co(OH)_2$/G250 hybrid flowers.

To better understand the structure and the composition of the hybrid flowers further, a series of measurements was performed on the product by heat treatment at 800 °C in air. All the diffraction peaks in the XRD pattern Figure 1c were assigned to the pure spinel Co_3O_4 with the *fcc* phase (JCPDS Card No. 74-1657). The Co_3O_4 product still has the hierarchical flower-like structure composed of abundant nanosheets after calcination as shown in the SEM image in Figure 2h. However, it seems that the Co_3O_4 nanosheets were fragile and fall off from the flowers. The high magnification SEM image in Figure 2i clearly reveals the porous structure and cracks appear on the surface of nanosheets, resulting from the decomposition of cobalt hydroxide and dye G250. Furthermore, the two narrow bands at 659 and 575 cm^{-1} in the FTIR spectrum (Supporting Information, Figure S2c) are the characteristic Co-O vibrations of Co_3O_4,[27] no obvious vibration bands due to the dye G250 are detected anymore after calcination at 800 °C. The fragile porous structures of the Co_3O_4 nanosheets are confirmed by the TEM image (Supporting Information, Figure S4). However, after calcination, the structure of the mesocrystal nanosheets disappeared in the HRTEM image but the single-crystal electron diffraction pattern is still observed. In view of above analysis, it can be concluded that the dye G250 molecules were indeed included in the β-$Co(OH)_2$ hybrids and dispersed with the $Co(OH)_2$ nanoparticles to induce the formation of mesocrystal sheets.

It was further investigated if the coexistence of CTAB and G250 was necessary to form the uniform β-$Co(OH)_2$/G250 flowerlike particles. A large number of unordered nanoparticle aggregates are obtained, if only G250 or CTAB was added in the reaction solution (Supporting Information, Figure S5). The above two products were Co_3O_4 according to the diffraction peaks of the XRD patterns (Supporting Information, Figure S6). Based on the above results, it was obvious that the synergistic effect of G250 and CTAB plays a crucial role not only for the morphology but also for the phase of the products.

Among the selected raw materials, CTAB was a positively charged surfactant, while G250 contained the sulfonate groups with the negative charges. In this way, the stable CTAB-G250 complex was theoretically formed through ionic self-assembly in the solution,[22a,28] which was confirmed by a large number of micelle-like aggregates with a diameter of about 150 nm (Supporting Information, Figure S7a). Following the addition of cobalt precursor into the water/ethanol solution, irregular

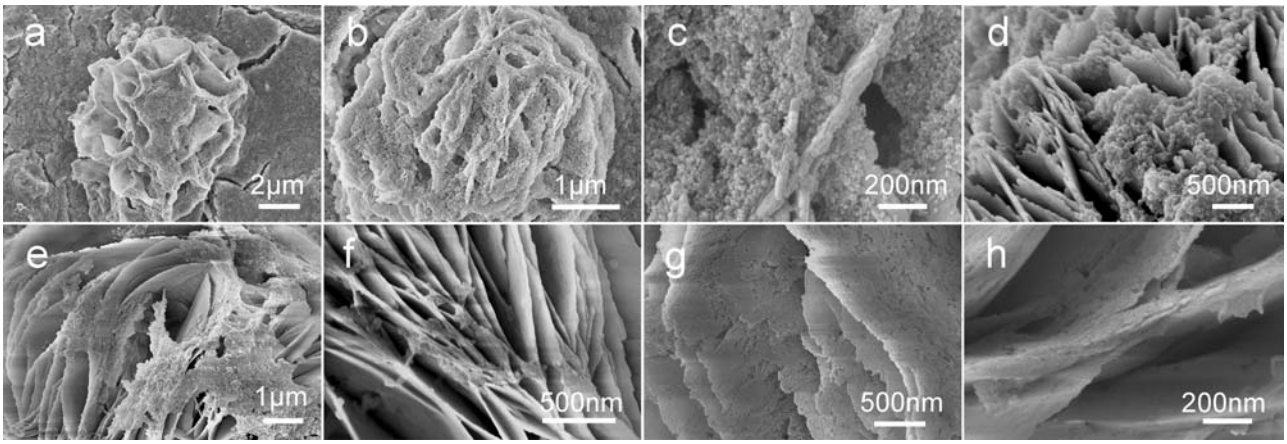

Figure 3. SEM images of the time-dependent evolution in the form of β-$Co(OH)_2$/dye hybrid flowers. (a) 1 h; (b and c) 3 h; (d) 6 h; (e) 12 h; (f and g) 24 h; (h) 36 h. The gradually disappearing nanoparticles (NPs) are shown as marked.

aggregates precipitated, which is attributed to the strong interaction between cobalt ions and hydrophilic sulfonate groups of the CTAB-G250 complex (Supporting Information, Figure S7b). The formation of the β-$Co(OH)_2$/dye hybrids with flower morphology is due the soft-templating effect of CTAB-G250 aggregates.

In order to reveal the formation mechanism of the flowery β-$Co(OH)_2$/dye hybrids, the SEM images and the XRD patterns based on the time-dependent evolution process were carried out, respectively. The morphology evolution of the product is shown in the SEM images in **Figure 3**. When the reaction proceeded to 1 h, the SEM image shows the embryonic structure with a size of about 10 μm and thick aggregates of nanoparticles dispersed in its surroundings. With the reaction time prolonged to 3 h, the earlier flowerlike product composed of the layered sheets is observed in Figure 3b. A mass of the thick nanoparticles is filled into the spaces between the sheets as clearly shown by a closer observation in the SEM image of Figure 3c. At this stage, the sheets are quite thick, the size of which was in the range of 60-80 nm. With prolonging of the reaction time to 6 h and 12 h, corresponding to the SEM images of Figure 3d and 3e, respectively, the small nanoparticles between the sheets disappeared gradually and grew together with the sheets. At the same time, the nanosheets became thinner and denser. When the reaction time increased to 24 h, only a slight amount of particles exists on the surface of the flower, no obvious particles are found on the rough nanosheets by the high-magnified SEM image (Figure 3g). With the reaction time increased to 36 h, the mesoporous β-$Co(OH)_2$/G250 flower with the thin nanosheets formed finally.

The XRD patterns of the intermediate samples at different reaction time are shown to reveal the component evolution during the formation of the β-$Co(OH)_2$/dye hybrids (Supporting Information, Figure S8). The XRD pattern of the weakly-crystallized sample centrifugated from the solution after the addition of all the reagents at room temperature could not be indexed according to the JCPDS cards. However, based on the analyses of the TEM image (Supporting Information, Figure S7) and the XRD pattern of the pure G250 in Figure 1a, we speculate that it is the complex of cobalt and CTAB-G250. The XPS survey spectrum of the corresponding sample showed the existence of cobalt, carbon, nitrogen and sulfur with contents of 8.5, 60.1, 3.4 and 2.0 at.%, respectively (Supporting Information, Figure S9), confirming the above speculated composition. The XRD patterns at different stages revealed the gradual transformation of the Co_3O_4 phase marked with black dots to β-$Co(OH)_2$. When the reaction time increases to 36 h, the diffraction peaks of Co_3O_4 disappear completely, exhibiting the β-$Co(OH)_2$ phase.

The combination of the evolution process based on the time-dependent SEM images and the XRD patterns for the formation of the flowerlike β-$Co(OH)_2$/G250 composites, the large number of the nanoparticles in the surrounding of the flowers formed at earlier stage are reasonable to be assigned as Co_3O_4, which serves as the reservoir for the further growth of β-$Co(OH)_2$. It well follows the typical Ostwald ripening process as a main driving force for the crystal growth.[10,11d] In the initial stage, β-$Co(OH)_2$ is formed and prone to crystallize into an unripened hexagonal mesocrystal aggregate composed of the stable and intrinsic platelets in alkaline solution.[29] The Co_3O_4 phase also simultaneously exists in the product, due to the thermodynamically favorable oxidation of cobalt treated with air.[17a] Along with the reaction proceeding, the small particles with their high surface energy tend to dissolve and recrystallize onto the original platelets. However, the phase transformation of the Co_3O_4 occurs with the evolution of the morphology simultaneously, which is due to the reduction of Co^{3+} to Co^{2+} by alcohol under ammonia atmosphere through the long-time refluxing process at 140 °C.[11b,19] Finally, the Co_3O_4 nanoparticles are completely consumed and the numerous thin nanosheets are assembled in a flower-like shape to minimize the surface energy and achieve the most stable state. In the meantime, the inclusion of the dye G250 within the nanosheets also stabilized such hierarchical structures. Herein, it is interesting that the phase transformation and morphology evolution occurs simultaneously in the formation of the flowery composites during the Ostwald ripening process.

Based on the above analysis, the formation process of the mesostructured β-$Co(OH)_2$/G250 flowers is proposed in **Scheme 1**. Firstly, the micelle-like aggregates are formed in the solution through the charge interactions of G250 and CTAB,

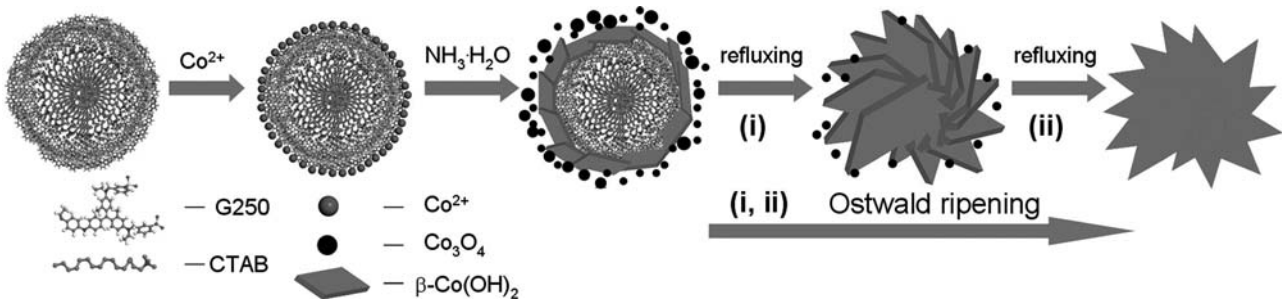

Scheme 1. Schematic illustration of the formation of β-$Co(OH)_2$/G250 hybrid flowers.

which serve as the soft templates to strongly interact with cobalt precursors. Then, free dye-stabilized nanoparticle-intermediates are formed and induce the formation of β-$Co(OH)_2$ mesocrystal nanosheets, which assemble around the micelle-like G250-CTAB complex and form the initial unripened flower morphology. With the reaction proceeding, small Co_3O_4 nanoparticles which are simultaneously formed to β-$Co(OH)_2$ due to partial oxidation of Co^{2+} in solution are sacrificed and grown onto the bulk nanosheets through Ostwald ripening mechanism after Co^{3+} ions got reduced in the ethanol/amine mixture upon prolonged refluxing. Finally, the well-defined flower-like β-$Co(OH)_2$/G250 hybrid structure is produced, where the included dye G250 exists around the nanoparticle-intermediates of the β-$Co(OH)_2$nanosheets and stabilizes the porous network of mesocrystal sheets.

A series of the UV-Vis absorption spectra in **Figure 4**A were measured on the as-prepared samples dispersed in ethanol against the same solvent as the blank at wavelengths ranging from 400-800 nm. The dye G250 is ethanol soluble, showing a well-defined peak at 611 nm in Figure 4A(a). For the other samples, the measurements were performed after the washing ethanol was colorless after repeated centrifugation. In the UV-Vis spectrum of Figure 4A(b), no obvious absorption peak is seen, the sample which was prepared with the addition of CTAB alone. If only G250 was used in the reaction, the spectrum displays a wide red-shifted peak at 638 nm in Figure 4A(c), indicating the inclusion of dye with inorganic cobalt compounds. Under the synergistic effect of CTAB and G250, the flowery β-$Co(OH)_2$/G250 solid has a blue color, which is obviously different from the violet G250. The peak in the spectrum of Figure 4A(d) is distinctly red-shifted 46 nm to 657 nm, resulting from the interactions between dye and β-$Co(OH)_2$. It can be seen that such hybrid material shows new optical properties distinct from the pure dye, confirming the real incorporation into the hybrid material, not just the simple mixture of the dye.

Figure 4B shows the time-dependent UV-vis spectra of the samples prepared at different stages. Interestingly, the red-shift trend from 620 nm to 657 nm is clearly observed in the UV-vis spectra with the reaction time prolonging from 1 h to 36 h. The data is well in accordance with the gradual component evolutions of Co_3O_4 to $Co(OH)_2$ obtained from the XRD patterns (see Supporting Information, Figure S9). According to crystal field theory, the higher-valent metal coordinates with the same ligand are, the higher splitting energy will be. Thus, followed by the transformation of Co^{3+} to Co^{2+} in the reaction, the splitting energy of cobalt ions interacting with G250 decreased, leading to the peak red-shifted in the UV-vis spectra, which further confirmed the existence of dye G250 in the mesostructured hybrids.

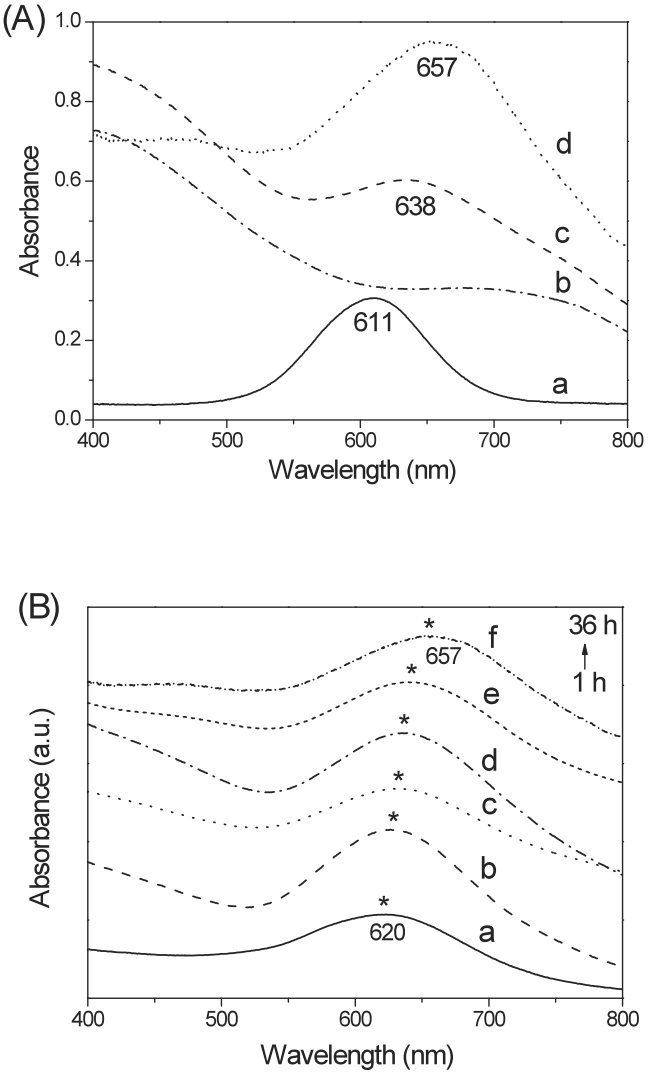

Figure 4. (A) UV-Vis spectra of (a) dye G250; (b,c) the sample synthesized in the presence of CTAB and G250, respectively; (d) β-$Co(OH)_2$/dye hybrid flowers. (B) UV-Vis spectra of the time-dependent evolution in the form of β-$Co(OH)_2$/dye hybrid flowers. (a) 1 h; (b) 3 h; (c) 6 h; (d) 12 h; (e) 24 h; (f) 36 h.

The flower-shaped β-$Co(OH)_2$/G250 hybrids show a good electrochemical response to oxygen reduction reaction (ORR) from the polarization curves using the rotating-disk electrode (RDE) (Supporting Information, Figure S10). The voltammogram plot obtained in a N_2-saturated solution suggests that the material is electrochemically inactive under these conditions. While saturated with O_2, the peak current is greatly increased, suggesting the obvious catalytic activity towards the ORR. Furthermore, the peak currents improve obviously followed by increasing the rotation rates, which is attributed to more oxygen diffusing to the surface of the electrode with higher rotation rates. A group of parallel and well-linear plots at different potentials as observed from the Koutecky–Levich (KL) plots (j^{-1} vs. $\omega^{-1/2}$) indicates the first-order kinetics on the dissolved oxygen.[30] The number of exchanged electrons of the composites in the ORR process is close to 3, as calculated from the slope of the K-L plots, which suggests that the reduction of O_2 on the catalysts proceeds simultaneously through the 4- and 2-electron transfer pathways.[31] To some extent, the well-defined electrocatalytic performance of the flowerlike β-$Co(OH)_2$/G250 for ORR depend on the mesoporous structure with a quite high surface area.

In summary, a new kind of β-$Co(OH)_2$/G250 hybrids with hierarchical structures composed of mesocrystal nanosheets can be conveniently synthesized by the soft-templating effect of the CTAB-G250 complex through ionic self-assembly via a one-step refluxing reaction. The dye G250 stabilizes and induces the formation of the mesocrystal β-$Co(OH)_2$ sheet building units of β-$Co(OH)_2$/G250 flower-shaped particles. Based on a series of time-dependent measurements, the formation mechanism of this functional hierarchical material has been investigated, which is well in accordance with the Ostwald ripening process. More importantly, this hybrid material exhibits new optical properties and obviously an electrochemical catalytic activity for ORR. The present synthetic route may allow to access other new inorganic-organic functional materials with potential applications in photoelectric and pigment fields.

Experimental Section

Preparation of β-Co(OH)$_2$/G250 hybrids: All the chemicals are of analytical grade and used without further purification. In a typical experiment, 1 mmol (0.249 g) of $Co(CH_3COO)_2{\cdot}4H_2O$ was added into 40 mL water/ethanol solution with 1:1 volume ratio. Then, 0.1 mmol (0.036 g) hexadecyl trimethyl ammonium bromide (CTAB) and 0.05 mmol (0.042 g) G250 were dissolved in the solution. With the addition of 10 mL $NH_3{\cdot}H_2O$, the flask was placed in an oil bath and the reaction mixture was refluxed at 140 °C for 36 h under stirring. After the solution was cooled to room temperature, the resulting products were centrifuged, washed with ethanol until the washing solution was colorless and dried at 60 °C.

Characterization: The X-ray diffraction (XRD) analysis was performed on a PW1710 instrument with CuKα radiation $\lambda = 0.15406$ nm. Scanning electron microscope (SEM) images were taken with a Zeiss Supra 40 scanning electron microscope at an acceleration voltage of 5 kV. Transmission electron microscope (TEM) images, HRTEM and SEAD pattern were examined by a JEOL-2010 microscope at an acceleration voltage of 200 kV. The X-ray photoelectron spectrum (XPS) was tested on an ESCALab MKII X-ray photoelectron spectrometer using Mg Ka radiation exciting source. Thermal gravimetric analysis (TGA) was carried out with a TA SDTQ 600 thermal analyzer, with a heating rate of 10 °C min^{-1} in air. The BET measurement was determined by using Micromeritics ASAP-2000 nitrogen adsorption apparatus. FTIR spectra were measured on a Bruker Vector-22 FTIR spectrometer from 4000–400 cm^{-1} at room temperature. UV-Vis spectra were recorded on a Shimadzu UV-240 spectrophotometer scanning from 400 to 800 nm at room temperature.

Electrochemical measurements: The electrochemical measurements were carried out using a rotating disk working electrode of glass carbon (PINE, 5 mm diameter, 0.2 cm^2) connected to a Multipotentiostat (IM6ex, ZAHNER elektrik, Germany). A platinum foil (1.0 cm^2) and Ag/AgCl (3 M) were used as the counter and reference electrodes, respectively. Then, the catalyst was dispersed in ethanol by sonication to get a suspension with 0.1 mg/mL catalyst. 10 µL of the suspension was transferred to the GCE and then 4 µL of 0.02 wt% Nafion (diluted from 5 wt% Nafion, Sigma-Aldrich) was added to the GCE. The catalytic activity was measured in 0.1 M KOH solutions at a scan rate of 20 mV/s bubbled with N_2 or O_2.

Acknowledgements

This work is supported by the National Basic Research Program of China (2010CB934700), the National Natural Science Foundation of China (Nos. 21001099, 91022032, 21061160492, J1030412), the International Science & Technology Cooperation Program of China (2010DFA41170), and the Principle Investigator Award by the National Synchrotron Radiation Laboratory at the University of Science and Technology of China. H. P. C. thanks the Fundamental Research Funds for the Central Universities, China Postdoctoral Science Foundation (20110490086), and the Foundation for the Author of Excellent Doctoral Dissertation of CAS.

[1] a) M. Vidotti, M. R. Silva, R. P. Salvador, S. I. C. de Torresi, L. H. Dall'Antonia, *Electrochim. Acta* **2008**, *53*, 4030; b) M. Dinamani, P. V. Kamath, *J. Appl. Electrochem.* **2000**, *30*, 1157.
[2] a) L. Cao, F. Xu, Y. Y. Liang, H. L. Li, *Adv. Mater.* **2004**, *16*, 1853; b) J. K. Chang, C. M. Wu, I. W. Sun, *J. Mater. Chem.* **2010**, *20*, 3729.
[3] a) M. S. Yarger, E. M. P. Steinmiller, K. S. Choi, *Chem. Commun.* **2007**, 159; b) T. D. Keene, M. E. Light, M. B. Hursthouse, D. J. Price, *Dalton Trans.* **2011**, *40*, 2983.
[4] a) R. Ma, Z. Liu, K. Takada, K. Fukuda, Y. Ebina, Y. Bando, T. Sasaki, *Inorg. Chem.* **2006**, *45*, 3964; b) P. V. Kamath, G. H. Annal Therese, J. Gopalakrishnan, *J. Solid State Chem.* **1997**, *128*, 38.
[5] H. S. Zhou, D. L. Li, M. Hibino, I. Honma, *Angew. Chem. Int. Ed.* **2005**, *44*, 797.
[6] J. Yang, H. Hyodo, K. Kimura, T. Sasaki, *Nanotechnology* **2010**, *21*, 045605.
[7] E. Hosono, S. Fujihara, I. Honma, H. S. Zhou, *J. Mater. Chem.* **2005**, *15*, 1938.
[8] X. W. Lou, D. Deng, J. Y. Lee, J. Feng, L. A. Archer, *Adv. Mater.* **2008**, *20*, 258.
[9] J. T. Sampanthar, H. C. Zeng, *J. Am. Chem. Soc.* **2002**, *124*, 6668.
[10] C. Xu, J. Sun, L. Gao, *Cryst. Eng. Commun.* **2011**, *13*, 1586.
[11] a) B. Li, Y. Xie, C. Wu, Z. Li, J. Zhang, *Mater. Chem. Phys.* **2006**, *99*, 479; b) L. X. Yang, Y. J. Zhu, L. Li, L. Zhang, H. Tong, W. W. Wang,

G. F. Cheng, J. F. Zhu, *Eur. J. Inorg. Chem.* **2006**, 4787; c) S. Xiong, C. Yuan, M. Zhang, B. Xi, Y. Qian, *Chem. Eur. J.* **2009**, *15*, 5320; d) R. Qiao, X. L. Zhang, R. Qiu, J. C. Kim, Y. S. Kang, *Chem. Eur. J.* **2009**, *15*, 1886.

[12] a) H. Cölfen, M. Antonietti, *Angew. Chem. Int. Ed.* **2005**, *44*, 5576; b) H. Cölfen, S. Mann, *Angew. Chem. Int. Ed.* **2003**, *42*, 2350; c) H. Cölfen, M. Antonietti, *Mesocrystals and Nonclassical Crystallization*, (John Wiley & Sons, Chichester) **2008**.

[13] a) M. Kijima, Y. Oaki, H. Imai, *Chem. Eur. J.* **2011**, *17*, 2828; b) M. Niederberger, H. Cölfen, *Phys. Chem. Chem. Phys.* **2006**, *8*, 3271; c) Z. P. Zhang, H. P. Sun, X. Q. Shao, D. F. Li, H. D. Yu, M. Y. Han, *Adv. Mater.* **2005**, *17*, 42; d) D. Gebauer, A. Verch, H. G. Boerner, H. Cölfen, *Cryst. Growth Des.* **2009**, *9*, 2398.

[14] a) J. Fang, B. Ding, X. Song, *Appl. Phys. Lett.* **2007**, *91*; b) T. D. Nguyen, D. Mrabet, T. T. D. Vu, C. T. Dinh, T. O. Do, *Cryst. Eng. Comm.* **2011**, *13*, 1450; c) A. Baynton, T. Radomirovic, M. I. Ogden, C. L. Raston, W. R. Richmond, F. Jones, *Cryst. Eng. Comm.* **2011**, *13*, 109; d) R. Q. Song, A. W. Xu, M. Antonietti, H. Cölfen, *Angew. Chem. Int. Ed.* **2009**, *48*, 395; e) R. Q. Song, H. Cölfen, A. W. Xu, J. Hartmann, M. Antonietti, *ACS Nano* **2009**, *3*, 1966.

[15] a) S. E. Wolf, J. Leiterer, V. Pipich, R. Barrea, F. Emrnerling, W. Tremel, *J. Am. Chem. Soc.* **2011**, *133*, 12642; b) I. C. Romero-Ibarra, G. Rodriguez-Gattorno, M. F. Garcia-Sanchez, A. Sanchez-Solis, O. Manero, *Langmuir* **2010**, *26*, 6954; c) V. M. Yuwono, N. D. Burrows, J. A. Soltis, R. L. Penn, *J. Am. Chem. Soc.* **2010**, *132*, 2163.

[16] M. E. Davis, *Nature* **2002**, *417*, 813.

[17] a) Y. Li, B. Tan, Y. Wu, *J. Am. Chem. Soc.* **2006**, *128*, 14258; b) Y. Li, B. Tan, Y. Wu, *Nano Lett.* **2008**, *8*, 265.

[18] G. Wang, H. Liu, J. Horvat, B. Wang, S. Qiao, J. Park, H. Ahn, *Chem. Eur. J.* **2010**, *16*, 11020.

[19] S. Tang, S. Vongehr, Y. Wang, L. Chen, X. Meng, *J. Solid State Chem.* **2010**, *183*, 2166.

[20] a) G. Wang, X. Shen, J. Horvat, B. Wang, H. Liu, D. Wexler, J. Yao, *J. Phys. Chem. C* **2009**, *113*, 4357; b) J. Zheng, J. Liu, D. Lv, Q. Kuang, Z. Jiang, Z. Xie, R. Huang, L. Zheng, *J. Solid State Chem.* **2010**, *183*, 600.

[21] a) H. Cölfen, S. H. Yu, *MRS Bull.* **2005**, *30*, 727; b) S. H. Yu, *Top. Curr. Chem.* **2007**, *271*, 79; c) A. B. Descalzo, R. Martínez-Máñez, F. Sancenón, K. Hoffmann, K. Rurack, *Angew. Chem. Int. Ed.* **2006**, *45*, 5924; d) H. Imai, *Top. Curr. Chem.* **2007**, *270*, 43; e) H. P. Cong, S. H. Yu, *Curr. Opin. Colloid Interface Sci.* **2009**, *14*, 71.

[22] a) H. P. Cong, S. H. Yu, *Adv. Funct. Mater.* **2007**, *17*, 1814; b) H. P. Cong, S. H. Yu, *Adv. Funct. Mater.* **2008**, *18*, 195.

[23] L. M. Qi, H. Cölfen, M. Antonietti, *Angew. Chem. Int. Ed.* **2000**, *39*, 604.

[24] Z. P. Xu, H. C. Zeng, *Chem. Mater.* **1999**, *11*, 67.

[25] Z. A. Hu, Y. L. Xie, Y. X. Wang, L. J. Xie, G. R. Fu, X. Q. Jin, Z. Y. Zhang, Y. Y. Yang, H. Y. Wu, *J. Phys. Chem. C* **2009**, *113*, 12502.

[26] a) R. Xu, H. C. Zeng, *J. Phys. Chem. B* **2003**, *107*, 12643; b) Y. L. Hou, H. Kondoh, M. Shimojo, T. Kogure, T. Ohta, *J. Phys. Chem. B* **2005**, *109*, 19094.

[27] a) T. He, D. R. Chen, X. L. Jiao, *Chem. Mater.* **2004**, *16*, 737; b) B. Pejova, A. Isahi, M. Najdoski, I. Grozdanov, *Mater. Res. Bull.* **2001**, *36*, 161.

[28] a) C. F. J. Faul, M. Antonietti, *Adv. Mater.* **2003**, *15*, 673; b) L. M. Qi, J. Li, J. M. Ma, *Adv. Mater.* **2002**, *14*, 300.

[29] B. Salvadori, L. Dei, *Langmuir* **2001**, *17*, 2371.

[30] N. M. Markovic, H. A. Gasteiger, P. N. Ross, *J. Phys. Chem.* **1995**, *99*, 3411.

[31] a) L. Xu, Y.-S. Ding, C.-H. Chen, L. Zhao, C. Rimkus, R. Joesten, S. L. Suib, *Chem. Mater.* **2008**, *20*, 308; b) Z. X. Liu, Z. P. Li, H. Y. Qin, B. H. Liu, *J. Power Sources* **2011**, *196*, 4972.